metals

MDPI

Article

Strength Prediction of Spherical Electronic Cabins with Pitting Corrosion

Hao Wang, Yongmei Zhu *, Xialei He, Wei Guan, Ming Zhan and Jian Zhang

Jiangsu University of Science and Technology, Zhenjiang 212003, China; wanghao@stu.just.edu.cn (H.W.); hexialei@stu.just.edu.cn (X.H.); guanwei@stu.just.edu.cn (W.G.); zhanming@just.edu.cn (M.Z.); zhjian127@just.edu.cn (J.Z.)

* Correspondence: zymtt@just.edu.cn

Abstract: In this paper, strength prediction of spherical electronic cabins with pitting corrosion under external pressure was investigated. The finite element model of a spherical electronic cabin with random pitting was established using self-written code. The effects of the pitting distribution shape, pitting morphology and size on the ultimate buckling load were numerically studied. In addition, the analytical formula for predicting the ultimate load of spherical cabin with random pitting corrosion was proposed and verified by experiments. This study can be used by engineering designers for relevant design and evaluation basis and provides a reference for the development of a new design code for the buckling stability of spherical cabins with pitting corrosion.

Keywords: pitting corrosion; buckling load; random; spherical electronic cabin; ultimate strength

Citation: Wang, H.; Zhu, Y.; He, X.; Guan, W.; Zhan, M.; Zhang, J. Strength Prediction of Spherical Electronic Cabins with Pitting Corrosion. *Metals* **2022**, *12*, 1120. https://doi.org/10.3390/met12071120

Academic Editor: George A. Pantazopoulos

Received: 19 May 2022
Accepted: 27 June 2022
Published: 29 June 2022

1. Introduction

The exploration and exploitation of the ocean has gradually shifted from shallow sea to deep sea [1]. Underwater experimental devices have been successfully placed at the seafloor by submersibles to automatically measure and record data electronically [2]. There are still many experiments and scientific studies that require the placement of electronic devices at the seafloor and their prolonged residence at the seafloor, such as the monitoring of submarine earthquakes and the monitoring of the hydrological environment [3–5]. But these electronic devices are non-pressure equipment, they are often installed into the pressure cabin and then placed in the ocean [6].

However, the deep sea environment is characterized by high pressure, intense salinity, sediments, sea mud, and a wide variety of animals, plants, and microorganisms. This extreme environmental characteristic has strict requirements on the high pressure and corrosion resistance of the pressure electronic cabin [2]. Among them, corrosion severely affects the life of electronic cabins on the seabed. For pressure electronic cabins that work under the sea for a long time, in addition to uniform corrosion, local corrosion (also known as non-uniform corrosion) is one of the common and extremely harmful corrosion. Severe local corrosion may greatly reduce the load-bearing capacity of the structure and cause serious safety accidents. Therefore, it is necessary to study the effect of local corrosion on the load-bearing capacity of the pressure electronic cabin [7].

Pit corrosion, as a typical structural local corrosion problem of structures, has been studied extensively by domestic and foreign scholars. It is important to study the emergence and development of pitting pits for studying pit corrosion. The growth of pitting pits in the marine environment is subject to a combination of factors, which poses great challenges for research. Different opinions on how to establish the growth and distribution model of corrosion pits have been proposed by some scholars. Melchers [8–10] processed the maximum pitting depth into an extreme value distribution. He proposed a probability distribution model of the maximum pitting depth and a five-stage model of pitting depth growth for low carbon steel in the marine submerged environment. Moreover, he illustrated

the process of structural reliability analysis considering the effects of pitting with a pipeline example. Wang et al. [10,11] established a new maximum depth model of pitting corrosion in the form of Weibull-function according to the observed data of real sea corrosion tests of carbon steel and low alloy steel commonly used in ship structures. They also established a time-dependent model of the pits ratio, based on the model of corrosion pits depth and the corrosion data of hold frames in cargo holds from literatures. They expressed the growth of corrosion pits with equations, which provided a reference for the numerical simulation.

The most important effect of local pitting is to reduce the structural load-bearing capacity, and scholars from various countries have done a lot of research on this. Ye et al. [12] combined the artificially accelerated corrosion test data of steel members, which made appropriate assumptions on the depth, diameter and distribution of pit holes. They proposed a simplified analytical method for the quantitative evaluation of the mechanical properties of steel members with pitting corrosion resistance by equivalent elastic modulus. Flaks [13] and Paik [14] studied the effects of pit corrosion on the ultimate strength of tensioned aluminum plates and ships. They concluded that the loss of cross-sectional area due to pit corrosion is a more significant indicator of interest than the depth of pit corrosion when assessing structural strength. Smith [15], Jiang [16], MacKay [17], et al., investigated the influence of local corrosion-induced thinning of pressure cabin shell on structural instability by experimental and numerical methods. Xu [18] studied the equivalent material constants of pitted corrosion plates and derived a finite element calculation method for cabins with pitted corrosion based on linear elasticity theory. Ma et al. [19] took a ring-ribbed cylindrical cabin subjected to pitting damage as the object of study adopted the single-variable method (SVM), and analyzed the effects of pitting pit depth, diameter, distribution location and density on the ultimate strength based on finite element analysis. They found that the corrosion pit density has little effect on the ultimate load. Ahn et al [20,21] have conducted axial pressure tests with circular pipes containing uniform corrosion and random pitting. They found that, within a certain range, the ultimate strength of circular pipes with pitting corrosion was closely related to the width, height and equivalent cross-section of the corrosion damage. Mokhtari [22] and Yu [23] studied the effect of localized pitting on structural strength. They separately established a strength decay equation for column cabins with localized pitting to make predictions for the residual strength of column cabins with pitting defects.

In summary, scholars have done many studies about the effect of local corrosion on the strength of pressure structures, especially the effect of local pitting, which includes pitting pit depth, diameter, density, and the randomness of pitting. Some have also proposed prediction equations for the strength of an electronic cabin with local pitting damage. However, a large number of studies have been focused on columnar cabins, while few studies have been conducted on spherical electronic cabins. The spherical electronic cabin is a common structural form of electronic cabins [24,25]. In extreme marine environments, the location, shape, and area of random pitting damage distribution on the external surface of the electronic cabin have obvious uncertainties. However, existing codes do not consider the effect of pitting defects' randomness when assessing the pressure resistance of spherical electronic cabins, which provides more conservative assessment results. Therefore, it is necessary to establish an effective pitting modeling method to characterize the pitting randomness and predict the buckling of external pressure spherical cabins with localized random pitting defects.

In this paper, the spherical cabin working at depths of 11,000 m was designed. The finite element model of spherical electronic cabin with random pitting was established using the self-written program, and nonlinear buckling of spherical cabin with pitting was studied. The effects of the pitting distribution shape, pitting morphology and size on the ultimate buckling load was investigated by numerical method. In addition, an analytical formula for predicting the ultimate load of spherical cabin with random pitting was proposed. Through testing, it is verified that this formula can predict the ultimate load of the pressure spherical cabin well.

2. Finite Element Model of Spherical Electronic Cabins with Local Random Pitting Defects

2.1. Structure Dimensions and Corrosion Parameters of the Spherical Electronic Cabin

This paper takes the spherical electronic cabin as the study object. Its working environment is 11,000 m in the deep sea, and the material is maraging steel. The material's elastic modulus E = 182 GPa, Poisson's ratio v = 0.3 and allowable stress is 1800 MPa. The calculated load is

$$p_s = k\rho_w gH/0.9 \tag{1}$$

where k is the safety factor; ρ_w is the density of sea water; g is the acceleration of gravity, and H is the depth of sea water. The electronic cabin runs smoothly during work, so where K is 1.45, ρ_w = 1.04 g/cm^3, g = 9.8 m/s^2, and H = 11,000 m. Through calculation, the load of the spherical electronic cabin at a water depth of 11 km is 180.62 MPa.

Then, the thickness of the spherical electronic cabin is

$$t_0 = \frac{p_s \times R}{2\sigma_\varphi} \tag{2}$$

where R is the spherical cabin's outer radius, σ_φ is the mid-surface stress, σ_φ = 1800 MPa, and the thickness of the spherical cabin is 10 mm. The dimensions and material properties of the spherical cabin are shown in Table 1. Its model is shown in Figure 1. The pitting depth is t, the pitting diameter is d, the pitting pit distribution location is determined by the corrosion angles θ_1 and θ_2, and the number of pits is denoted as N_{pit}.

Table 1. Spherical cabin design size and material performance.

Name	Parameters
Outside diameter D_0 (mm)	430
Cabin thickness t_0 (mm)	10
Young's modulus E (MPa)	182,000
Poisson's ratio ν	0.3

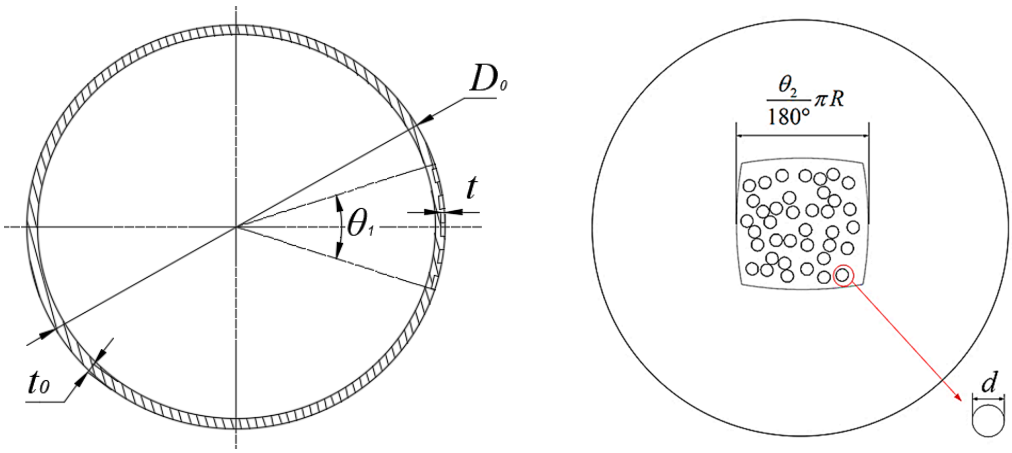

Figure 1. Spherical electronic cabin with local random pitting defect (N_{pit} = 36).

2.2. Numerical Model of Spherical Electronic Cabins with Local Random Pitting Defects

The actual corrosion of ocean steel structures is similar to a kind of uneven thickness corrosion, in which pitting corrosion is the main form. The shape, location and depth of pitting corrosion damage are completely random [26]. To simulate practical engineering problems, a numerical model of a spherical pressure cabin with random pitting defects is needed. Wang et al. [27] established random corrosion model of steels plates, in which pitting pits were cylindrical, and evaluated the effect of random pitting on galvanized structural steel. In the study of the collapse pressure of cylindrical cabins with random

pitting corrosion, Wang et al. [28,29] established a model of randomly corroded cylindrical cabins to study the effect of pitting pits on rupture pressure of deep-sea pipeline under external pressure. The cylindrical cabin with random pitting corrosion can be built by this modeling method, but the spherical cabin with random pitting corrosion cannot be built. For the sake of simplification, this paper assumes that the local pitting corrosion of spherical electronic cabins in the marine environment is equivalent to a series of random pitting pits, each of which has the same section and depth, and each of which does not overlap. The ABAQUS (Dassault Systèmes, Velizi Vilacuble, France) script was written in Python language, and the modeling method of the spherical cabin with random spherical pits was established. The flowchart for the generation of random spherical pits is shown in Figure 2.

Step 1: Use Python language integrated development environment (IDE) to import Math, Random modules.

Step 2: The outer diameter of the spherical cabin was defined as D_0, the wall thickness was defined as t_0, the depth of pitting corrosion was defined as t, the pitting diameter d was $2t$, the pitting number was defined as N_{pit}, and the distribution area of pitting corrosion was $\theta_1 \times \theta_2$.

Step 3: Define m and n

$$m = \frac{\sqrt{2(\frac{D_0}{2})^2(1-\cos\frac{\theta_1 \cdot 180}{\pi})}}{2} - t$$

$$n = \frac{\sqrt{2(\frac{D_0}{2})^2(1-\cos\frac{\theta_2 \cdot 180}{\pi})}}{2} - t$$

Step 4: Define the coordinates of pitting center (x,y,z)

$$x = (-m, m)$$

$$y = (-n, n)$$

$$z = \sqrt{(\frac{D_0}{2})^2 - x^2 - y^2}$$

Step 5: The pitting spherical centers' x, y, and z coordinates were generated using the random statement. These pitting centers were located on the outer sphere of the spherical cabin.

Step 6: Use the while statement to control the number of pitting pits to N_{pit}

Step 7: Use the list statement to calculate the distance between the centers of any two pitting spheres. When the distance between two pitting was less than $2t$, one of them would be deleted.

Step 8: Check for convergence:
If $N < N_{pit}$, THEN
$N = N + 1$
Go to Step 5
ELSE
Go to Step 9

Step 9: Running by ABAQUS, and generate the spherical cabin model with random pitting.

Figure 2. Flowchart of random spherical pits generation.

The spherical electronic cabin geometric model and pitting pits geometric model were established in the ABAQUS/Part module respectively. The spherical electronic cabin and pitting pits were then assembled in the ABAQUS/Assemble module. Finally, the geometric model of pitting pits was used as a cutting tool, and the spherical electronic cabin geometry model was used as the cutting object. The geometric model of the spherical electronic cabin with pitting defects was created by excision with Boolean operations. The geometric model of spherical electronic cabin with random pitting defects is shown in Figure 3.

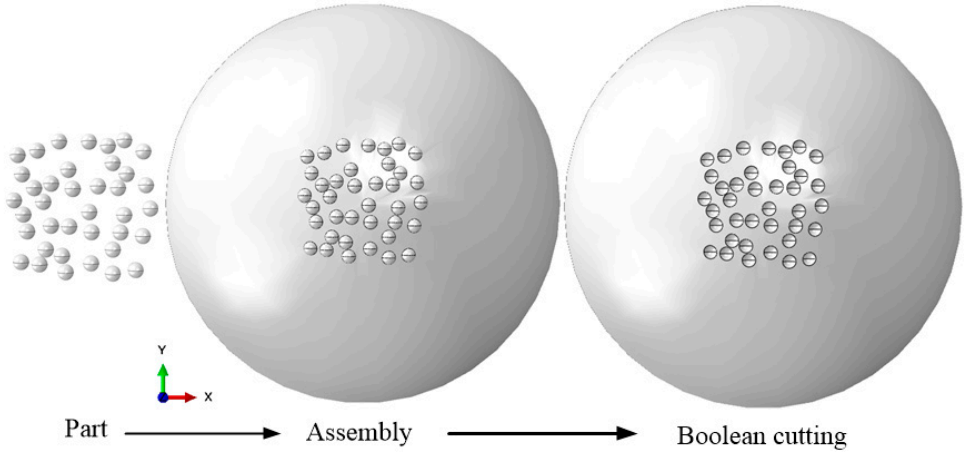

Figure 3. Geometric model of spherical electronic cabin with local random pitting defects.

The geometric complexity of the pitting area of the spherical electronic cabin model was considered, so tetrahedral free meshes were adopted. In the ABAQUS/Mesh module, the spherical cabin was divided into two parts. The part containing pitting defects was divided into C3D10 mesh using an adaptive mesh generation algorithm. The part without pitting defects was divided into C3D8R mesh using a structure division algorithm to simplify the operation and ensure the quality of the mesh. The finite element model of the spherical electronic cabin with local random pitting damage is shown in Figure 4.

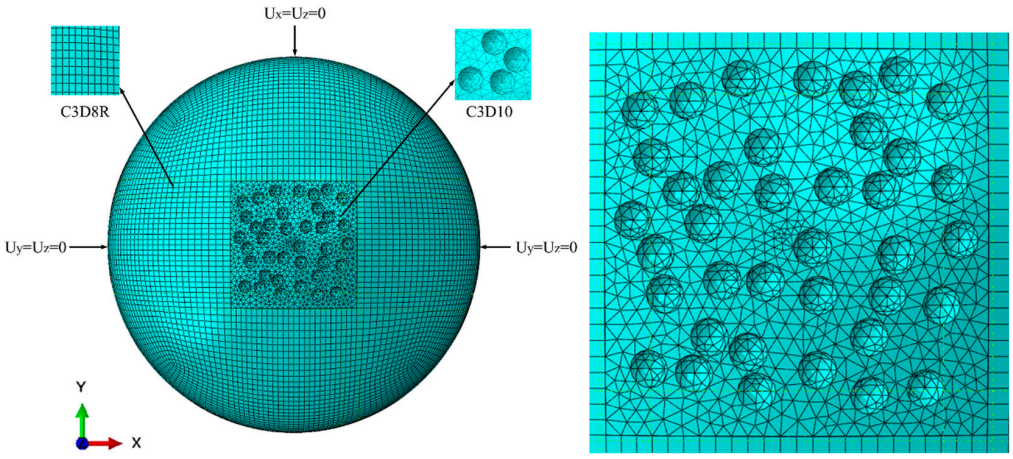

Figure 4. Finite element model of spherical electronic cabin with local random pitting defects.

2.3. Nonlinear Buckling Analysis

The Riks analysis was used to analyze the nonlinear buckling of the pressure electronic cabin with pitting defects. Because the object of finite element analysis is the spherical electronic cabin with pitting defects, pitting pits were used to replace the initial flaws. With reference to specification ENV1993-1-6 (2007), all nonlinear buckling analyses were set. The error of nonlinear buckling analysis of ideal and real elastic-plastic material models is very small [30]. Therefore, to simplify the calculation, the ideal elastoplastic was used as the yield criterion of the material.

The spherical electronic cabin is in the sea when it is working. The outer part of the spherical cabin is subjected to uniform external pressure from seawater, so the degrees of freedom of the spherical cabin itself are not restricted. However, to eliminate rigid body motion, the degrees of freedom of the spherical cabin still must be limited in the process of establishing the finite element model. Three points were used to limit its six directional degrees of freedom; that is, three nodes were taken at the position 90° apart from the x-axis and y-axis to limit two-directional degrees of freedom. The constraints were as follows:

Uy = Uz = 0, Uy = Uz = 0, and Ux = Uz = 0. The constraint reaction force of each point was close to 0, indicating that the constraints imposed were reasonable and limited only the rigid body displacement of the model. The boundary conditions are shown in Figure 4.

3. Influence of Corrosion Defect Parameters

3.1. Influence of Pitting Distribution Shape on the Buckling Behavior of Spherical Cabins

The corrosion distribution shape of spherical electronic cabin under normal operation is different. This section studies the influence of different distribution shapes on the residual ultimate strength of spherical electronic cabins under the same area and the same number of random pitting pits.

Since the local pitting corrosion of spherical electronic cabins is studied, the range of corrosion angles in both directions of longitude and latitude is set as 10° to 60°, and four sets of solutions are set:

(1) θ_1 =60° and θ_2 = 10°;
(2) θ_1 =40° and θ_2 = 15°;
(3) θ_1 =30° and θ_2 = 20°;
(4) θ_1 =24.5° and θ_2 = 24.5°;

According to the corrosion regulations of bulk carrier warehouses, the corrosion depth for pitting or grooving in the side shell, hopper tank and topside tank plating attached to the cargo hold side frame is less than 70% of the as-built thickness [31]. Considering the actual situation, the pit depth in this paper was selected at 4 mm and 6 mm (t/t_0 = 0.4, 0.6), and the number of pitting pits was chosen at 16 and 36. The pit shape was spherical. The Riks method in ABAQUS software (Dassault Systèmes, Velizi Vilacuble, France) was used for analysis, and the specific setting is described in Section 2.2. The buckling load under different pitting distribution shapes is shown in Table 2.

Table 2. Buckling load of spherical electronic cabins under different pitting distribution shape (MPa); the values in parentheses are normalized by the uncorroded spherical cabins buckling loads.

N_{pit}	t/t_0	60° × 10°	40° × 15°	30° × 20°	24.5° × 24.5°
0	0	187.110(1)			
16	0.4	174.142 (0.931)	171.335 (0.916)	168.972 (0.903)	163.328 (0.873)
	0.6	142.207 (0.760)	139.608 (0.746)	135.565 (0.725)	132.099 (0.706)
36	0.4	160.022 (0.855)	156.997 (0.839)	153.969 (0.823)	150.698 (0.805)
	0.6	120.193 (0.642)	116.610 (0.623)	111.092 (0.594)	110.029 (0.588)

Figure 5 shows the effect of the pitting distribution shape ($\theta_1 \times \theta_2$) on the ultimate load of spherical electronic cabins with pitting defects. It can be seen from Figure 5 that the pitting distribution shapes have similar effects on the buckling load of spherical cabins under different pitting numbers and pit depths. The longer the distribution shape of pitting corrosion, the smaller the decrease in buckling load. The closer the distribution shape of pitting corrosion to a square, the more significant the reduction in the buckling load. This indicates that when the pitting distribution shape is square, the ultimate load of the spherical electronic cabin with pitting corrosion is significantly affected. Therefore, the pitting corrosion in the square distribution area is used in the subsequent research in this paper so that the values obtained are more conservative.

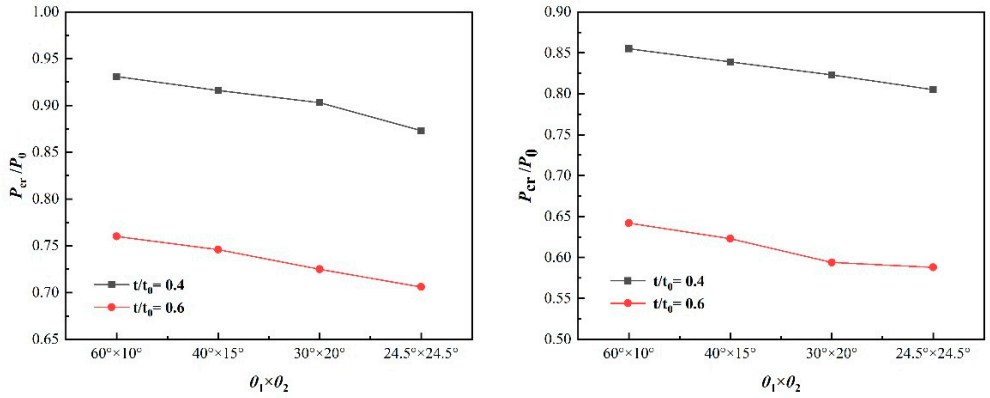

Figure 5. Influence of pitting distribution shape on the buckling load of spherical cabins. (**a**) N_{pit} = 16; (**b**) N_{pit} = 36.

3.2. Influence of Pitting Morphology on the Buckling Behavior of Spherical Electronic Cabins

Generally, the pits formed in local corrosion are discrete pits of various shapes. Zhang et al. [31] found that the morphology of pitting corrosion did not affect the ultimate strength of stiffened plates. Yu et al. [32] found that the collapsing pressure of the corrosion ring was influenced not only by the mass loss and the minimum residual wall thickness but also by the actual shape of the pits, but its influence is limited. However, these are studies of the ultimate strength of the flat plate by pitting morphology. In this section, the finite element model of spherical, ellipsoidal, cylindrical and rectangular pitting pits with the same volume is established to study the influence of different pitting morphology on the buckling load of spherical electronic cabins under the same volume.

Here, the pit depth t was taken as 2 mm, 3 mm, 4 mm, 5 mm, and 6 mm (t/t_0 = 0.2, 0.3, 0.4, 0.5, 0.6), and the influence of pitting pits with four morphological parameters on the buckling load of spherical cabins was studied. In the case of the spherical pit, the pit depth t is its radius, and the volume of the spherical pit can be determined to be $\frac{2}{3}\pi t^3$. Because of the same volume, the volume of ellipsoidal, cylindrical and rectangular pits should be approximately $\frac{2}{3}\pi t^3$. The geometric parameters of pitting pits in four forms are shown in Figure 6. When the pit depth is also t, the dimensions of single pitting pits are shown in Table 3.

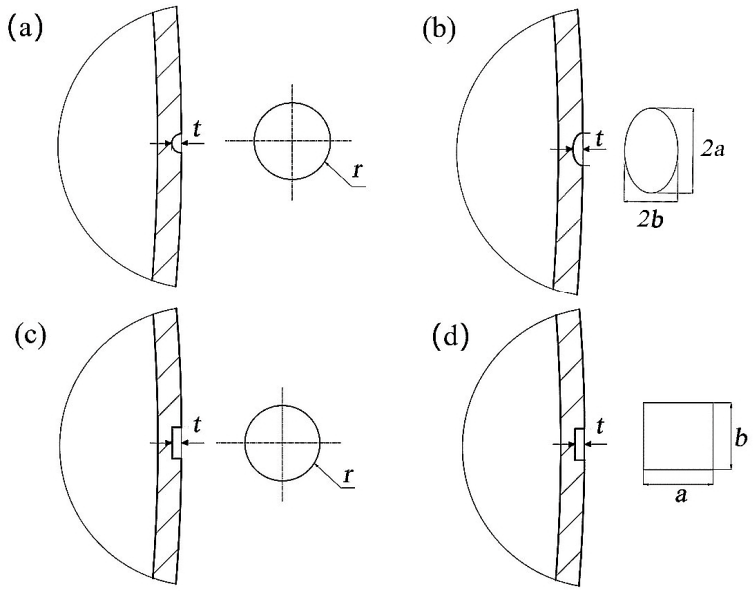

Figure 6. Geometric parameters of pitting pits in four forms. (**a**) Spherical (**b**) elliptical (**c**) cylindrical (**d**) rectangular.

Table 3. Size parameters of single pitting pits.

Corrosion Depth	Morphology	Geometric Parameter (mm)	Volume (mm^3)
$t/t_0 = 0.2$	Spherical	$r = 2$; $t = 2$	16.755
	Ellipsoid	$a = 2.5$; $b = 1.6$; $t = 2$	16.755
	Cylindrical	$r = 1.633$; $t = 2$	16.755
	Rectangular	$a = 2.894$; $b = 2.894$; $t = 2$	16.750
$t/t_0 = 0.3$	Spherical	$r = 3$; $t = 3$	56.549
	Ellipsoid	$a = 4.5$; $b = 2.25$; $t = 3$	56.549
	Cylindrical	$r = 2.449$; $t = 3$	56.526
	Rectangular	$a = 4.341$; $b = 4.341$; $t = 3$	56.533
$t/t_0 = 0.4$	Spherical	$r = 4$; $t = 4$	134.041
	Ellipsoid	$a = 5$; $b = 3.2$; $t = 4$	134.041
	Cylindrical	$r = 3.266$; $t = 4$	134.042
	Rectangular	$a = 5.789$; $b = 5.789$; $t = 4$	134.050
$t/t_0 = 0.5$	Spherical	$r = 5$; $t = 5$	261.799
	Ellipsoid	$a = 6.25$; $b = 4$; $t = 5$	261.799
	Cylindrical	$r = 4.083$; $t = 5$	261.866
	Rectangular	$a = 7.236$; $b = 7.236$; $t = 5$	261.798
$t/t_0 = 0.6$	Spherical	$r = 6$; $t = 6$	452.389
	Ellipsoid	$a = 8$; $b = 4.5$; $t = 6$	452.389
	Cylindrical	$r = 4.899$; $t = 6$	452.393
	Rectangular	$a = 8.683$; $b = 8.683$; $t = 6$	452.367

Here, the pitting number was set as 36, and the pitting distribution area was chosen at $60° \times 60°$. The finite element analysis results are shown in Table 4 and Figure 7.

Table 4. Buckling load of spherical cabins under different pitting morphologies (MPa); the values in parentheses are normalized by the uncorroded spherical cabin buckling loads.

Corrosion Depth	Spherical	Ellipsoid	Cylindrical	Rectangular
0	**187.11(1)**			
$t/t_0 = 0.2$	178.90 (0.956)	178.96 (0.956)	178.94 (0.956)	178.81 (0.956)
$t/t_0 = 0.3$	177.23 (0.947)	177.35 (0.948)	176.97 (0.946)	176.69 (0.944)
$t/t_0 = 0.4$	172.77 (0.923)	172.80 (0.924)	172.38 (0.921)	172.76 (0.923)
$t/t_0 = 0.5$	162.56 (0.869)	164.41 (0.879)	160.15 (0.856)	162.52 (0.869)
$t/t_0 = 0.6$	151.69 (0.811)	152.86 (0.817)	151.44 (0.809)	152.00 (0.812)

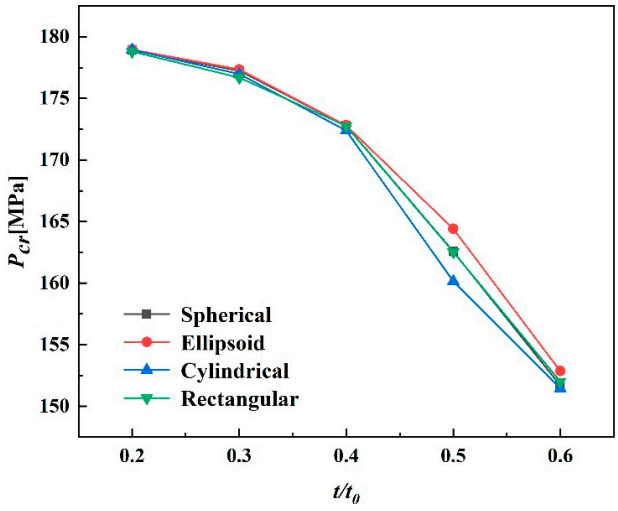

Figure 7. Influence of pitting morphology on the buckling load of spherical cabins at different pit depths.

From Table 4, it is found that there is little difference in the effect of various corrosion pit shapes on the buckling load of spherical cabins with pitting defects. When the corrosion depth (t/t_0) is 0.4, the difference is the largest. At this stage, the spherical cabin under the ellipsoidal pit has the largest residual ultimate buckling strength (164.41 MPa), while the spherical cabin under the cylindrical pit has the smallest residual ultimate buckling strength (160.15 MPa), and the difference between them is 2.59%. Zhang et al. [31] obtained similar results, and they found that the difference between the effect of cylindrical and conical corrosion pits on the strength of stiffened rib plates was only 1%. When the corrosion depth (t/t_0) is less than 0.4, rectangular pitting pits have the greatest effect on the spherical cabin buckling load; when the corrosion depth (t/t_0) is greater than or equal to 0.4, cylindrical pitting pits have the greatest effect on the spherical cabin buckling load. It is of interest that ellipsoidal pitting pits have less effect on the spherical cabin buckling load than any other shape of pitting pits under the same conditions. Therefore, it is conservative to use ellipsoidal pitting pits to simulate the effect of corrosion on ultimate loads. In addition, as shown in Figure 7, when the corrosion depth (t/t_0) is less than 0.4, the buckling load of the pressure spherical cabin with pitting defects decreases more slowly with the corrosion depth. When the corrosion depth (t/t_0) exceeds 0.4, the ultimate load of the pressure spherical cabin with pitting corrosion declines sharply with the corrosion depth. In summary, the corrosion pits shape has little effect on the ultimate buckling load of the spherical electronic cabin. The corrosion depth has more influence on the ultimate buckling load of the spherical electronic cabin and needs to be paid more attention to.

In summary, equal to the rectangular steel plate with pitting defects, the spherical electronic cabin with pitting defects is not sensitive to the shape parameters of pitting pits. This indicates that when studying the effect of pitting on the remaining ultimate strength of spherical electronic cabins, it is reliable to model the pitting morphology by simplifying it to the cylindrical or spherical cavity, which effectively reduces the modeling difficulty and simplifies the calculation.

3.3. Influence of Pitting Dimensions on the Buckling Behavior of Spherical Cabins

Pitting pits are very small compared with the whole deep-sea spherical electronic cabin and are often covered by corrosion products, making them difficult to detect. The ultimate load of spherical electronic cabins under different sizes of pitting defects is explored in this section. Here, the number of pits was taken as 36; the area of pitting distribution was chosen as $60^\circ \times 60^\circ$; and the morphology of pitting craters was set as cylindrical. The depths of the pitting pits (t/t_0) were set at 0.2, 0.3, 0.4, 0.5 and 0.6; the ratio of diameter to depth (d/t) of pitting pits was set at 1, 2, 3 and 4. The results of the finite element analysis are shown in Table 5.

Table 5. Buckling loads of spherical cabins under pitting pits with different diameter-depth ratios (MPa); the values in parentheses are normalized by the uncorroded spherical cabin buckling loads.

Corrosion Depth (t/t_0)	Diameter to Depth Ratio (d/t)			
	1	**2**	**3**	**4**
0	**187.11(1)**			
0.2	186.560 (0.997)	185.417 (0.991)	183.177 (0.979)	181.220 (0.969)
0.3	185.692 (0.992)	181.325 (0.969)	175.516 (0.938)	167.625 (0.896)
0.4	183.503 (0.981)	173.848 (0.929)	159.324 (0.851)	144.215 (0.771)
0.5	180.113 (0.963)	161.202 (0.862)	137.178 (0.733)	120.729 (0.645)
0.6	177.440 (0.948)	145.931 (0.780)	109.354 (0.584)	89.086 (0.476)

Table 5 shows that the size of pitting pits had a significant influence on the buckling load of spherical cabins with local pitting defects. An increase in pitting depth or diameter led to a decrease in the residual ultimate buckling load of spherical cabins with local pitting

defects. Figure 8 shows the effect of corrosion depth (t/t_0) and the diameter-to-depth ratio of the pitting crater (d/t) on the ultimate load of the spherical electronic cabin.

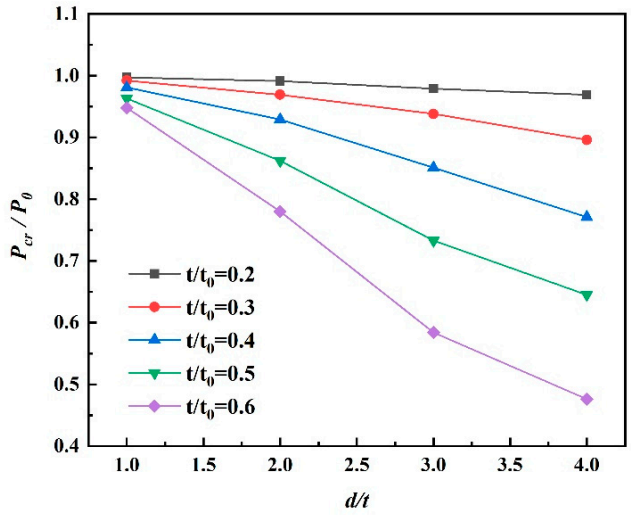

Figure 8. Ultimate load of spherical electronic cabins under pitting of different sizes.

Figure 8 shows that with an increase in the diameter of the pitting pits with a large corrosion depth, the ultimate load of the spherical electronic cabin decreased sharply. At $t/t_0 = 0.6$ and $d/t = 4$, the limit load of the spherical cabin with local pitting corrosion decreased by 52.4%. However, when the corrosion depth was small, the limit load decreased more slowly. At $t/t_0 = 0.2$, even when the pit diameter increased to $d/t = 4$, the ultimate load of the spherical electronic cabin also decreased by only 3.1%. When the corrosion pit diameter was small ($d/t = 1$) and the corrosion depth increased from 2 mm to 6 mm, the ultimate buckling load of the spherical electronic cabin decreased by 4.9%. However, when the diameter of the corrosion pits was large ($d/t = 4$) and the corrosion depth increased from 2 mm to 6 mm, the ultimate buckling load of the spherical electronic cabin decreased by 49.3%.

In summary, the influence of the size of pitting pits on the ultimate load of spherical electronic cabins can be expressed by two parameters: corrosion depth (t/t_0) and diameter-depth ratio (d/t). On the one hand, when the total area of pitting pits was the same, the ultimate buckling load of spherical electronic cabins was basically the same. For example, the ultimate buckling load of spherical cabins containing 36 pitting pits with diameters of 4 mm was 183.50 MPa (row 6, column 2 in Table 5), while that of spherical cabins containing 16 pitting pits with diameters of 6 mm was 181.62 MPa. The difference in ultimate buckling load between them was only 1%. This shows that the influence of pitting pit diameter and pitting number on the ultimate load of the spherical electronic cabin can be described by the total pitting area. On the other hand, when the total corrosion volume was nearly the same (row 7, column 5 and row 8, column 4 in Table 5), the ultimate buckling load of spherical electronic cabins was 10.76% different. Therefore, the influence of pitting size on the residual ultimate strength of spherical cabins with pitting defects can be regarded as the influence of area loss and depth loss caused by pitting on the ultimate residual strength of spherical electronic cabins.

4. Prediction of Ultimate Load of a Spherical Cabin with Local Random Pitting Defects

In this section, the section damage rate A_{loss} and the relative depth of pitting t/t_0 are selected as parameters to study the ultimate buckling load of spherical cabins with random pitting defects. The expression for the cross-sectional damage rate A_{loss} is

$$A_{loss}\% = \frac{1}{S_{\theta_1 \times \theta_2}} \sum_{i=1}^{N_{pit}} A_i \times 100\% \quad (3)$$

where $S_{\theta_1 \times \theta_2}$ is the area of the pitting distribution area, and A_i is the surface area of the ith pitting.

Section damage rate A_{loss} describes the ratio of the surface area of pitting damage to the area of pitting distribution. As shown in Figure 9, the black dots in the figure indicate the area of pitting damage, which is determined by the diameter d of the pitting and the number of pits N_{pit}; in addition, the area in the dashed box is the area of the pitting distribution area. To simplify the calculation, pitting in the square distribution area is used in this section for the calculation.

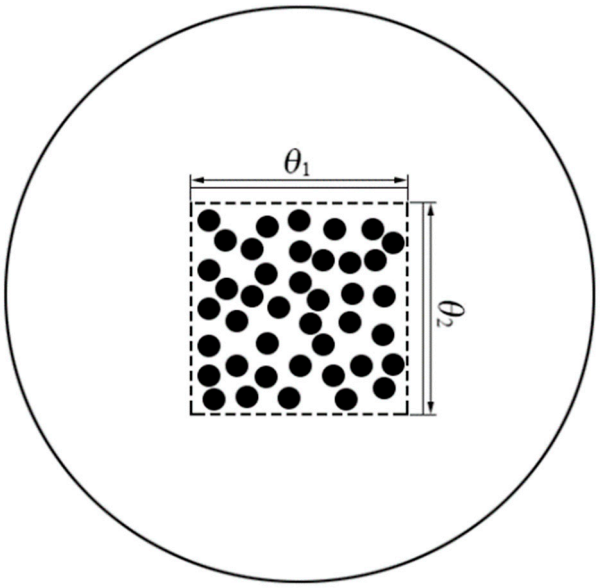

Figure 9. Schematic diagram of A_{loss}.

To obtain the ultimate load of spherical cabins with random pitting defects more simply, it is necessary to deduce the analytical formula. The Zolley formula is the most classical theoretical formulation that considers only the buckling instability of the spherical cabin in the linear elastic phase of the material [33], which is shown in Equation (4):

$$p_{Zoelly} = 2E(t_0/r)^2/\sqrt{3(1-\nu^2)} \tag{4}$$

where E is Young's modulus, r is the median radius of the spherical cabin, t_0 is the wall thickness of the spherical cabin, and ν is Poisson's ratio.

In this paper, based on the Zolley formula, an analytical formula for nonlinear buckling of spherical cabins with local random pitting defects is derived by adding a defect factor, as shown in Equation (5):

$$P_u = k\frac{2\mathrm{E}}{\sqrt{3(1-v^2)}}(\frac{t_0}{r})^2 \tag{5}$$

where K is the defect factor.

Combining the analysis above with previous research, K can be expressed as

$$k = (\mathrm{a}_1 * (A_{loss})^3 + \mathrm{a}_2 * (A_{loss})^2 + \mathrm{a}_3 * A_{loss} + a_4) * (\frac{t}{t_0})^{a_5} * (\frac{t_0}{r})^{a_6} \tag{6}$$

To obtain the defect factors of the spherical cabin caused by random pitting defects, A_{loss} was selected as 10%, 20%, 30%, 40%, 50% and 60%; t/t_0 was chosen as 0.2, 0.25, 0.3, 0.35, 0.4, 0.45, 0.5, 0.55 and 0.6; and t_0/r was set as 0.01, 0.02, 0.03, 0.04, and 0.05. A total of $6 \times 9 \times 5 = 270$ spherical cabin models with random pitting defects were carried out for nonlinear numerical analysis. Figure 10 shows the defect factor, which is the ratio of

the nonlinear buckling load of a spherical cabin with random pitting defects to the linear buckling load of a perfect spherical cabin.

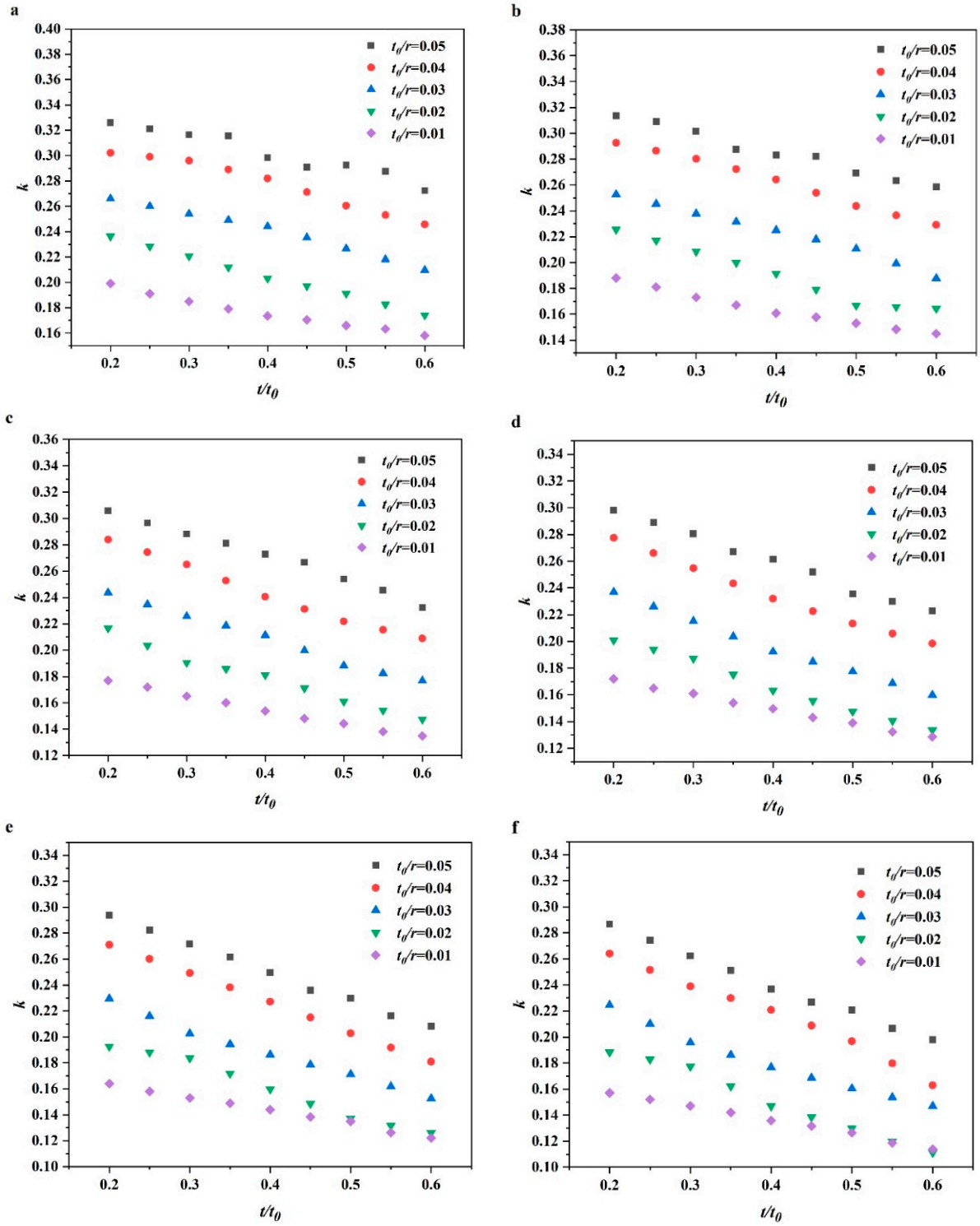

Figure 10. Defect factor k (**a**) A_{loss} = 10%; (**b**) A_{loss} = 20%; (**c**) A_{loss} = 30%; (**d**) A_{loss} = 40%; (**e**) A_{loss} = 50%; (**f**) A_{loss} = 60%.

To obtain a more accurate analytical formula, 270 numerical results were fitted by the least squares regression method [34] and MATLAB software (MathWorks, Massachusetts, MA, USA). The initial value was set to 1, and the output was $a_1 = -0.3118$; $a_2 = 0.5690$; $a_3 = -0.5310$; $a_4 = 0.6443$; $a_5 = -0.2723$ and $a_6 = 0.3248$.

5. Experimental Verification

To verify the above analytical formula for the ultimate load of spherical cabins with local random pitting defects, four stainless steel spherical cabins with the nominal diameter of 150 mm and the nominal thickness of 1 mm were designed and fabricated for verification. The spherical cabins were named #1, #2, #3 and #4. A Φ4*10*50L-55* cutter was used to mill the stainless steel spherical cabins, simulating the pitting corrosion produced by the corrosion [35]. The dimensions of these pits were as follows: pit diameter d = 4 mm, pit depth t = 0.5 mm. The spherical cabin model photos are shown in Figure 11.

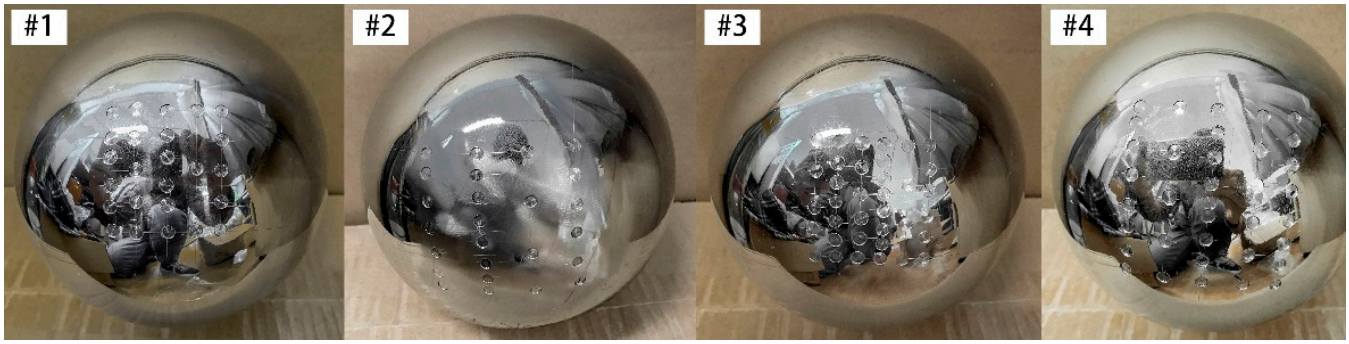

Figure 11. The specimen model; (**#1**) A_{loss} = 20.46%; (**#2**) A_{loss} = 9.19%; (**#3**) A_{loss} = 29.25%; (**#4**) A_{loss} = 13.22%.

The actual wall thickness t_0 and diameter D_0 of the spherical cabin with local random pitting defects were measured using an ultrasonic thickness gauge and coordinate measuring machine (CMM), respectively, prior to the hydraulic test. The average values are listed in Table 6. After geometrical measurements, all spherical cabins were hydrostatically tested in a pressure test chamber. Specific details of the measurements and tests can be found in the literature [36]. The material properties of the specimens were measured through the tensile test of the specimens, and they were yield strength σ_{yp} = 296.6 MPa, Young's modulus E = 199 GPa, and Poisson's ratio ν = 0.302. The hydrostatic pressure test results P_{test} are listed in column 6 of Table 6.

Table 6. Specimen parameters and measurement and test results.

	D_0 (mm)	Standard Deviation	t_0 (mm)	Standard Deviation	$\theta_1 \times \theta_2$	Number of Pits	P_{test} (MPa)	P_u (Equation (5)) (MPa)
#1	149.66	0.147	0.777	0.005	30° × 30°	25	4.07	3.69 (0.907)
#2	148.86	0.203	0.771	0.004	45° × 45°	25	4.21	3.96 (0.940)
#3	150.23	0.185	0.771	0.004	30° × 30°	36	3.17	3.43 (1.081)
#4	148.95	0.196	0.770	0.006	45° × 45°	36	4.18	3.84 (0.919)

The collapsed modes after the test are shown in Figure 12. The collapsed modes of all spherical cabins are identical and in the form of a local dent at pitting pits, which is caused by the high ductility of stainless steel and pitting defects on the cabin. It is also found that when the spherical cabin collapses, the local dents are almost symmetrically arranged along the welding seam. Therefore, it is evident that the geometric defects at the welding can cause great buckling changes. This shows that spherical cabins are very sensitive to geometric defects and that instability usually occurs at the local geometric imperfections of the spherical cabin.

The measured diameter, thickness, yield strength, Young's modulus and Poisson's ratio were used to verify the analytical calculation formula. According to the section damage rate, thickness-diameter ratio and corrosion depth of the four stainless steel spherical cabins, the ultimate buckling load of the four spherical cabins is predicted, as shown in Column 7 of Table 6. The ratio of the predicted buckling load to the test load is between 0.906 and

1.081, which shows that the predicted buckling load is in good agreement with the test results. Notably, most results of the formula are below the experimental values. This may be because the defect form in the formula considers not only the random pitting defects but also the initial geometric defects of the spherical cabin. The defect shape in the experiment is certain, and the actual defect may be less than the model defect. In addition, the influence of different materials on the buckling load of spherical cabins is neglected, which may affect the prediction results to a certain extent.

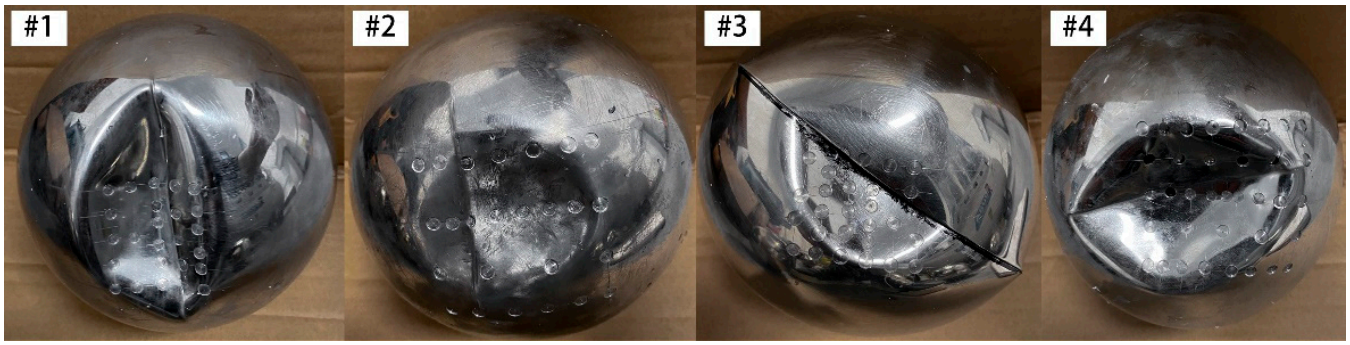

Figure 12. Views of the specimen after collapse by external hydrostatic pressure; (**#1**) A_{loss} = 20.46%; (**#2**) A_{loss} = 9.19%; (**#3**) A_{loss} = 29.25%; (**#4**) A_{loss} = 13.22%.

6. Conclusions

(1) The pitting diameter and depth have great influence on the ultimate buckling load of spherical cabin with pitting corrosion. When the pitting distribution tends to square, the residual ultimate load of spherical cabin decreases. In addition, the pitting morphology has no significant effect on the residual ultimate load of spherical cabin with pitting corrosion.

(2) The relative area loss A_{loss}, the relative depth of pitting corrosion t/t_0 and the ratio of thickness to diameter t_0/r are used as the parameters of buckling load and pitting damage for the spherical cabin with pitting corrosion, which are more reasonable than the corrosion volume.

(3) The nonlinear buckling loads of spherical cabins with pitting corrosion are calculated under different section damage rates, pitting relative depths and thickness-to-diameter ratios. A_{loss} is 10–60%, t/t_0 is 0.2–0.6, and t_0/r is 0.01–0.05. Combined with the Zoelly formula, an analytical formula is derived.

(4) The buckling load obtained by the analytical formula is close to the test result, and the difference is less than 10%. This formula can be used to predict the nonlinear buckling load of spherical cabins with pitting corrosion.

Author Contributions: H.W. and Y.Z. equally contributed to this work. Conceptualization, X.H.; methodology, W.G.; software, H.W.; Validation, M.Z. and J.Z. investigation, H.W. and Y.Z.; data curation, Y.Z. and H.W.; writing—original draft preparation, H.W.; writing—review and editing, Y.Z. All authors have read and agreed to the published version of the manuscript.

Funding: This work was supported by the Natural Science Foundation of Jiangsu Province [grant number BK20211343], The National Natural Science Foundation of China [grant number 52071160], and the State Key Laboratory of Ocean Engineering (Shanghai Jiao Tong University) (Grant No. GKZD010081).

Institutional Review Board Statement: Not applicable.

Informed Consent Statement: Not applicable.

Data Availability Statement: The data presented in this study are available on request from the corresponding author. The data are not publicly available due to privacy.

Conflicts of Interest: The authors declare no conflict of interest.

References

1. Dai, C.H.; Lao, X.S.; Liu, Y.; Wei, W. Experimental Study on Water-Lubricated Bearing Material in Deep Sea Space Station. *Mater. Sci. Forum* **2019**, *947*, 155–159. [CrossRef]
2. Liang, J.; Feng, J.-C.; Zhang, S.; Cai, Y.; Yang, Z.; Ni, T.; Yang, H.-Y. Role of deep-sea equipment in promoting the forefront of studies on life in extreme environments. *iScience* **2021**, *24*, 103299. [CrossRef] [PubMed]
3. Delaney, J.; Heath, G.; Chave, A.; Kirkham, H.; Howe, B.; Wilcock, W.; Beauchamp, P.; Maffei, A. NEPTUNE: Real-Time, Long-Term Ocean and Earth Studies at the Scale of a Tectonic Plate. In Proceedings of the MTS/IEEE Oceans 2001. An Ocean Odyssey. Conference Proceedings (IEEE Cat. No.01CH37295), Honolulu, HI, USA, 5–8 November 2001; Volume 3, pp. 1366–1373. [CrossRef]
4. Yang, C.; Xie, Q.C.; Ma, Q. A review of study on seafloor seismic observation network. *Seismol. Geomagn. Obs. Res.* **2017**, *38*, 161–167.
5. Lellouche, J.-M.; Greiner, E.; Le Galloudec, O.; Garric, G.; Regnier, C.; Drevillon, M.; Benkiran, M.; Testut, C.-E.; Bourdalle-Badie, R.; Gasparin, F.; et al. Recent updates to the Copernicus Marine Service global ocean monitoring and forecasting real-time 1/12° high-resolution system. *Ocean Sci.* **2018**, *14*, 1093–1126. [CrossRef]
6. Li, D.; Li, Y.; Ding, Z.; Wang, X.; Liu, B. Development and application of a temperature gradient detector for manned underwater robot. *Int. J. Adv. Robot. Syst.* **2020**, *17*, 1729881420916963. [CrossRef]
7. Xiang, Y.J.; Bian, R.G. Calculation method for stability of pressure hull with local corrosion. *J. Ship Mech.* **2017**, *21*, 61–68.
8. Melchers, R.E. Pitting Corrosion of Mild Steel in Marine Immersion Environment—Part 1: Maximum Pit Depth. *Corrosion* **2004**, *60*, 824–836. [CrossRef]
9. Melchers, R.E. Pitting Corrosion of Mild Steel in Marine Immersion Environment—Part 2: Variability of Maximum Pit Depth. *Corrosion* **2004**, *60*, 937–944. [CrossRef]
10. Wang, Y.W.; Huang, X.P.; Cui, W.C. Pitting corrosion model of mild and low-alloy steel in marine environment-Part 1: Maximum pit depth. *J. Ship Mech.* **2007**, *11*, 577–586.
11. Wang, Y.W.; Wu, X.Y.; Zhang, Y.H. Pitting corrosion model of mild and low-alloy steel in marine environment—Part 2: The shape of corrosion pits. *J. Ship Mech.* **2007**, *11*, 735–743.
12. Ye, J.H.; Shen, H.Q.; Xue, S.D. Simplified analytical method of mechanical property degradation for steel members with pitting corrosion. *J. Harbin Inst. Technol.* **2016**, *48*, 70–75.
13. Flaks, V.Y. Correlation of pitting corrosion of aluminum plates and reduction of load-bearing capacity under tension. *Mater. Sci.* **1978**, *14*, 75–78. [CrossRef]
14. Paik, J.K.; Lee, J.M.; Ko, M.J. Ultimate shear strength of plate elements with pit corrosion wastage. *Thin-Walled Struct.* **2004**, *42*, 1161–1176. [CrossRef]
15. Smith, M.J.; MacKay, J.R. Overall Elasto-Plastic Collapse of Ring Stiffened Cylinders with Corrosion Damage. *Int. J. Marit. Eng.* **2005**, *147*, A1–A54.
16. Jiang, L.; Limited, C.M.; Wallace, J.; Norwood, M.; MacKay, J.R.; Smith, M.J.; Bosman, T.N.; Atlantic, C.D.R.C. Finite Element Modeling of Collapse Experiments of Ring Stiffened Cylinders with Simulated Corrosion Damage. In Proceedings of the Warship 2008: Naval Submarines, Glasgow, UK, 10–11 June 2008. [CrossRef]
17. MacKay, J.R. *Experimental Investigation of the Strength of Damaged Pressure Hulls-Phase 1*; Defence Research and Development Canada-Atlantic: Ottawa, ON, Canada, 2007; p. 112.
18. Xu, Q.; Wan, Z.Q. Finite Element method of pitting corrosive shell. *J. Ship Mech.* **2010**, *14*, 84–93.
19. Ma, X.L.; Wu, F.; Zhang, E. Study on Ultimate Strength of Ring-stiffened Cylindrical Shell under Pitting Corrosion Damage. *Ship Ocean. Eng.* **2018**, *47*, 29–32+37.
20. Ahn, J.-H.; Choi, W.R.; Jeon, S.H.; Kim, S.-H.; Kim, I.-T. Residual compressive strength of inclined steel tubular members with local corrosion. *Appl. Ocean Res.* **2016**, *59*, 498–509. [CrossRef]
21. Ahn, J.-H.; Jeon, S.-H.; Jeong, Y.-S.; Cho, K.-I.; Huh, J. Evaluation of Residual Compressive Strength and Behavior of Corrosion-Damaged Carbon Steel Tubular Members. *Materials* **2018**, *11*, 1254. [CrossRef]
22. Mokhtari, M.; Melchers, R.E. Reliability of the conventional approach for stress/fatigue analysis of pitting corroded pipelines–Development of a safer approach. *Struct. Saf.* **2020**, *85*, 101943. [CrossRef]
23. Yu, J.X.; Jin, C.G.; Yu, Y. Plastic Collapse Capacity of 2D Ring with Internal Random Pitting Corrosion Defects. *J. Tianjin Univ. (Sci. Technol.)* **2019**, *52*, 1219–1226.
24. Hou, X.; Guo, S.; Shi, L.; Xing, H.; Yin, H.; Li, Z.; Zhou, M.; Xia, D. Improved Model Predictive-Based Underwater Trajectory Tracking Control for the Biomimetic Spherical Robot under Constraints. *Appl. Sci.* **2020**, *10*, 8106. [CrossRef]
25. Li, Y.S.; Sun, H.X. Design and Development of Small Spherical Underwater Observation Robot. *J. Mech. Eng.* **2020**, *56*, 103–109.
26. Sun, J.; Wang, R.H.; Dou, P.L. Stochastic finite element analysis of circular pipe members with inhomogeneous thickness corrosion damage. Chinese Society of Ocean Engineering: Ocean Engineering Branch of Chinese Society of Oceanography. In Proceedings of the 17th China Ocean (Shore) Engineering Symposium, Beijing, China, 2015; pp. 236–330.
27. Wang, R.; Shenoi, R.A.; Sobey, A. Ultimate strength assessment of plated steel structures with random pitting corrosion damage. *J. Constr. Steel Res.* **2018**, *143*, 331–342. [CrossRef]
28. Wang, H.; Yu, Y.; Yu, J.; Duan, J.; Zhang, Y.; Li, Z.; Wang, C. Effect of 3D random pitting defects on the collapse pressure of pipe—Part I: Experiment. *Thin-Walled Struct.* **2018**, *129*, 512–526. [CrossRef]
29. Wang, H.; Yu, Y.; Yu, J.; Jin, C.; Zhao, Y.; Fan, Z.; Zhang, Y. Effect of 3D random pitting defects on the collapse pressure of pipe—Part II: Numerical analysis. *Thin-Walled Struct.* **2018**, *129*, 527–541. [CrossRef]

30. Zhang, J.; Zhang, M.; Tang, W.X.; Wang, W.; Wang, M. Buckling of spherical shells subjected to external pressure: A comparison of experi-mental and theoretical data. *Thin-Walled Struct.* **2017**, *111*, 58–64. [CrossRef]
31. Zhang, Y.; Huang, Y.; Meng, F. Ultimate strength of hull structural stiffened plate with pitting corrosion damage under unaxial compression. *Mar. Struct.* **2017**, *56*, 117–136. [CrossRef]
32. Yu, J.; Wang, H.; Fan, Z.; Yu, Y. Computation of plastic collapse capacity of 2D ring with random pitting corrosion defect. *Thin-Walled Struct.* **2017**, *119*, 727–736. [CrossRef]
33. Zoelly, R. Ueber ein Knickungsproblem an der Kugelschale. Ph.D. Thesis, ETH Zürich, Zürich, Switzerland, 1915; pp. 1–146. [CrossRef]
34. Shi, W.Z.; Tong, L.W.; Chen, Y.Y. Experimental study of the effect of corrosion on the force performance of steel and steel beams. *J. Build. Struct.* **2012**, *33*, 53–60.
35. Sheng, J.; Xia, J. Effect of simulated pitting corrosion on the tensile properties of steel. *Constr. Build. Mater.* **2017**, *131*, 90–100. [CrossRef]
36. Zhu, Y.; Guan, W.; Wang, H.; Zhao, M.; Zhang, J. Buckling of spherical shells with pitting corrosion under external pressure. *Ships Offshore Struct.* **2021**, *12*, 1–10. [CrossRef]